Materials Advances

ROYAL SOCIETY OF CHEMISTRY

PAPER

View Article Online
View Journal | View Issue

Cite this: *Mater. Adv.*, 2026, 7, 3287

Carbon dioxide–sulphur hexafluoride adsorption and separation with zirconium metal–organic frameworks bearing basic and fluorinated linkers

Giacomo Provinciali,[a] Giulio Bicchierai,[a] Ferdinando Costantino,[b] Cristiano Zuccaccia,[b] Letizia Trovarelli,[bc] Lorenzo Donà,[c] Bartolomeo Civalleri,[c] Francesca Bonino,[c] Francesca Rosso,[c] Giuliano Giambastiani,[ade] Giulia Tuci[ae] and Andrea Rossin*[ae]

This study describes the synthesis and characterization of two novel zirconium-based mixed-linker metal–organic frameworks (MIXMOFs) of the UiO-6x family (**fcu** topology) containing basic and fluorinated linkers together in the same lattice: **Zr_TFA_NH$_2$**, built with 2-aminoterephthalic acid (H_2BDC-NH_2) and trifluoroacetic acid (HTFA) with minimal formula $[Zr_6O_4(OH)_4(TFA)_{4.2}(BDC\text{-}NH_2)_{3.9}]$ and **Zr_TFA_PyPy**, containing 2,2′-bipyridyl-4,4′-dicarboxylic acid (H_2PyPy) and HTFA with minimal formula $[Zr_6O_4(OH)_4(TFA)_{1.8}(PyPy)_{5.1}]$. The linkers are cheap and commercially available; they were selected to control pore size and functional group distribution: H_2BDC-NH_2 is a short linker and provides UiO-66-like smaller pores, while H_2PyPy is a longer linker and generates larger UiO-67-like pores. TFA^- acts both as modulator and fluorinated functional group source. The two MIXMOFs have been exploited for the adsorption and separation of carbon dioxide (CO_2) and sulfur hexafluoride (SF_6), two potent greenhouse gases. Isosteric heats of CO_2 adsorption (Q_{st}) are higher than those found in their non-fluorinated analogues, proving the synergistic adsorption enhancement from combining basic and fluorinated linkers in the same solid. SF_6/CO_2 selectivity values derived from competitive adsorption experiments of equimolar mixtures at ambient temperature and pressure indicated that **Zr_TFA_NH$_2$** is more efficient than **Zr_TFA_PyPy** in separating the two gases. Density functional theory (DFT) calculations were performed to identify primary adsorption sites and estimate binding energies; the calculated adsorption energies agree well with the experimental Q_{st} values.

Received 5th January 2026,
Accepted 16th February 2026

DOI: 10.1039/d6ma00018e

rsc.li/materials-advances

1. Introduction

Air pollution is a critical environmental challenge, with greenhouse gases playing a major role in climate change. The last 30th United Nations Climate Change Conference (COP30) held in Belém (Brazil) in November 2025[1] addressed various climate-related issues, including those pertaining to greenhouse gases. Addressing air pollution necessitates a multifaceted approach, combining technological innovation, robust policy frameworks and international collaboration. The outcomes of COP30 underscore the global commitment against climate change and the reduction of greenhouse gas emissions. Among these gases, carbon dioxide (CO_2) and sulfur hexafluoride (SF_6) are of particular concern due to their significant global warming potential. CO_2 is the primary greenhouse gas emitted by human activities, mainly from the combustion of fossil fuels such as coal, oil and natural gas. It is a key driver of global warming, as it traps heat in the Earth's atmosphere, leading to rising temperatures, extreme weather events and ecosystem disruptions. Efforts to mitigate CO_2 emissions focus on transitioning to renewable energy sources, improving energy efficiency, and developing carbon capture and storage technologies.[2] SF_6 is a synthetic gas widely used in the electrical industry for its excellent insulating properties in high-voltage equipment. However, SF_6 has an extremely high global warming potential (approximately 23 500 times that of CO_2 over a 100-year period) and can persist in the atmosphere for thousands of years. Despite its relatively low emission levels compared to CO_2, its

[a] *Istituto di Chimica dei Composti Organometallici (CNR-ICCOM), Via Madonna del Piano 10, Sesto Fiorentino (Firenze), 50019, Italy. E-mail: a.rossin@iccom.cnr.it*
[b] *Dipartimento di Chimica, Biologia e Biotecnologie e CIRCC, Università degli Studi di Perugia, via Elce di Sotto 8, 06123 Perugia, Italy*
[c] *Dipartimento di Chimica, Centro NIS, Unità di Ricerca INSTM, Università di Torino, Via G. Quarello 15/A and Via P. Giuria 7, I-10125 Torino, Italy*
[d] *Dipartimento di Chimica Ugo Schiff, Università di Firenze, Via della Lastruccia 3-13, 50019 Sesto Fiorentino (Firenze), Italy*
[e] *Consorzio Interuniversitario Nazionale per la Scienza e Tecnologia dei Materiali (INSTM), Via G. Giusti, 9, 50121 Firenze, Italy*

long atmospheric lifetime and potent greenhouse effect make it a major concern. Efforts to reduce SF_6 emissions involve finding alternative insulating gases, improving gas recovery techniques and enhancing equipment maintenance to minimize leaks.[3] An efficient approach to address the pollution caused by CO_2 and SF_6 and reduce their atmospheric concentrations (limiting their environmental impact) is their selective adsorption using porous solids. In particular, Metal–Organic Frameworks (MOFs) are a class of porous crystalline materials that have gained increasing attention in the last years in this context. MOFs are organic–inorganic compounds made by the combination of assorted metal nodes and polytopic organic linkers whose relevance in comtemporary chemistry has been brought to the attention of the worldwide news after the assigment of the Nobel Prize in Chemistry 2025 to Omar Yaghi, Susumu Kitagawa and Richard Robson for their pioneering work in this area.[4] Their highly tunable structures, exceptional surface areas and adjustable pore sizes make them ideal candidates for gas adsorption and separation applications.[5–8] In gas adsorption, MOFs exhibit superior capacity due to their well-defined porosity and high affinity toward specific gas molecules, often with remarkable gas uptake and release under mild conditions.[6] More specifically, MOFs offer a highly efficient platform for post-combustion (acidic) CO_2 capture when they contain amine-functionalized (or, more generally, basic groups) on their polar organic linkers that are able to engage with strong chemisorption interactions with CO_2.[9–13] Another class of MOFs that is being studied for the same application is that of fluorinated MOFs (F-MOFs). Fluorination enhances CO_2 adsorption because of the presence of the electronegative fluorine atoms that enhances dipole–quadrupole interactions with CO_2 molecules, increasing adsorption capacity. In addition, fluorination also reduces water interference in CO_2 adsorption, making F-MOFs highly effective in humid conditions.[14–21] MOFs have also shown excellent performance in SF_6 capture due to their hydrophobicity (SF_6, being a large, nonpolar molecule, interacts well with hydrophobic MOFs with large pore openings), high binding energy (the strong van der Waals interactions between SF_6 and MOFs enhance adsorption selectivity) and low-pressure capture efficiency (MOFs exhibit high SF_6 uptake even at low pressures).[22] Analogously to what has been described for CO_2, MOFs bearing basic groups on their linkers and/or fluorinated substituents are also very efficient in SF_6 adsorption. Since SF_6 is a weak Lewis acid, it can interact with basic groups present in the MOF structure, improving capture efficiency. At the same time, fluorine electronegativity increases SF_6 binding affinity through dispersion forces and quadrupole interactions. For gas mixture separation, MOFs leverage their selective adsorption capabilities to differentiate between gas molecules based on size, shape, and chemical interactions. This makes them highly effective in challenging separations. Separating CO_2 from SF_6 is particularly important in industrial processes where SF_6 is used, such as gas insulation systems, high-voltage equipment and semiconductor manufacturing. It often appears mixed with inert gases such as N_2 or CO_2 during use or waste streams. SF_6/CO_2 mixtures commonly used in electrical insulation applications have a composition around 20 mol% of SF_6 and 80 mol% of CO_2.[23] Recovery and separation of SF_6 from such mixtures is both an economic and environmental imperative (reuse of expensive SF_6 and reduction of emissions).[24] Conventional separation techniques, such as cryogenic distillation, are energy-intensive. Again, MOFs offer a promising alternative due to their ability to selectively adsorb one gas over the other. Recent research highlights that F-MOFs enhance SF_6 uptake *via* van der Waals and dispersion interactions making them highly selective for this gas,[25,26] while basic MOFs exploit Lewis base-acid interactions to adsorb SF_6, but often prefer CO_2 due to its higher quadrupole moment.[27,28] With this in mind and with the target of designing new MOFs for CO_2 and SF_6 adsorption/separation, in our labs we have adopted a ''hybrid'' strategy combining fluorination and basic functionalization within the same MOF that may optimize SF_6 or CO_2 capture performance while allowing tunable CO_2/SF_6 separation. Accordingly, two novel zirconium mixed-linker MOFs of UiO-6x (**fcu**) topology[29] built with the basic linkers 2-aminoterephtalic acid (H_2BDC-NH_2), [2,2′-bipyridine]-5,5′-dicarboxylic acid (H_2PyPy) and the fluorinated linker trifluoroacetic acid (HTFA, Scheme 1) have been synthesized and fully characterized: $[Zr_6O_4(OH)_4(TFA)_{4.2}(BDC\text{-}NH_2)_{3.9}]$ (**Zr_TFA_NH$_2$**) and $[Zr_6O_4(OH)_4(TFA)_{1.8}(PyPy)_{5.1}]$ (**Zr_TFA_PyPy**). Their performance in CO_2 and SF_6 adsorption/separation has been analyzed.

2. Experimental section

2.1. Materials and methods

Zirconium chloride ($ZrCl_4$), trifluoroacetic acid (HTFA), *N*,*N*-dimethylformamide (DMF), 2-aminoterephtalic acid (H_2BDC-NH_2) and [2,2′-bipyridine]-5,5′-dicarboxylic acid (H_2PyPy) were purchased from Sigma Aldrich and used as received. NMR experiments were performed using a Bruker 400 Avance III HD 400 instrument equipped with a smart probe (400.13 MHz

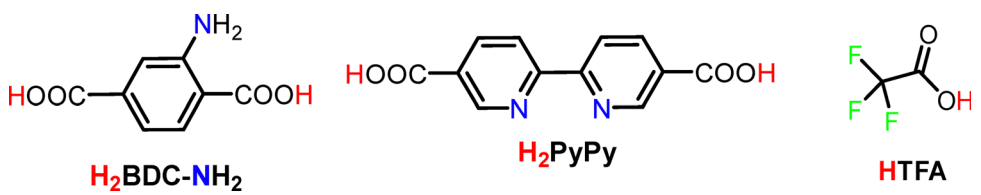

Scheme 1 The linkers used in this study for the construction of the Zr^{IV} MIXMOFs **Zr_TFA_NH$_2$** and **Zr_TFA_PyPy**: 2-aminoterephtalic acid (H_2BDC-NH_2), [2,2′-bipyridine]-5,5′-dicarboxylic acid (H_2PyPy) and trifluoroacetic acid (HTFA).

for ^{1}H) at T = 298 K. ^{1}H and ^{19}F NMR spectra were recorded using standard pulse sequences available on the Bruker library. Each sample was allowed to equilibrate inside the NMR probe for 10 min before spectral acquisition and each NMR spectrum was acquired using a single scan. ^{1}H and ^{19}F NMR chemical shifts were referenced to external HDO in D_2O by taking into account the γ_F/γ_H ratio for ^{19}F. As for the linker quantification in the solids, solutions of **Zr_TFA_NH$_2$** and **Zr_TFA_PyPy** were prepared by holding 5 mg of each MOF in an oven at T = 393 K for 2 h before being digested in 1.5 mL of D_2SO_4/D_2O(96 w/w%)/DMSO-d_6 solution kept at T = 298 K for 36 h and 24 h, respectively. For the calculation details, see SI and Fig. S1. FT-IR spectra (KBr pellets) were recorded on a PerkinElmer spectrum BX series FTIR spectrometer, in the 4000–400 cm^{-1} range, with a 2 cm^{-1} resolution. Thermogravimetric analyses (TG-DTG) were performed under a N_2 flow (100 mL min^{-1}) at a heating rate of 5 K min^{-1} with an EXSTAR Thermo Gravimetric Analyzer Seiko 6200. The latter was coupled with a ThermoStarTM GSD 301T mass spectrometer for mass analysis of the volatile species. The elemental analyses were performed using a Thermo FlashEA 1112 Series CHNS-O elemental analyzer with an accepted tolerance of ±2% on carbon (C), hydrogen (H) and nitrogen (N). Scanning electron microscopy and energy dispersive X-ray analysis (SEM-EDX) measurements were performed on a field emission-SEM TESCAN S9000G equipped with a Schottky-type EGF source. The voltage used for electron acceleration is 15 kV, and the probe current is 300 pA. An OXFORD model Ultim Max AZTEC software was used for the microanalysis. The nature and purity of all the batches employed for the functional characterization were assessed through powder X-ray diffraction (PXRD). PXRD qualitative measurements were carried out in the 2.0–50.0° 2θ region with a Panalytical X'PERT PRO diffractometer equipped with a Ni filter in the diffracted beam, a PIXcel© solid state detector and a sealed X-ray tube (Cu Kα, λ = 1.5418 Å). Slits were used on both the incident (soller slits aperture: 0.25°; divergence slit aperture: 0.5°) and the diffracted (anti-scatter slit aperture: 7.5 mm) beam. The generator was operated at 40 kV and 40 mA. PXRD patterns for structural analysis were collected with the same setup but in the 4°–90° 2θ region with a 50 sec per step. The samples were previously evacuated from solvent molecules at T = 393 K for 2 h. The breakthrough (BT) adsorption and desorption curves were measured with a BreakThrough Analyzer (BTA) instrument from Micromeritics®. BTA is equipped with one mass flow controller (MFC, Bronkhorst) for each gas; after the mixing of the desired flow, 1/32′ inch pipeline leads to a quartz reactor (37.0 cm length and 9.33 cm^3 of internal volume), axially inserted in a ceramic furnace. The reactor is equipped with two K type thermocouples (TC): one in contact with the sample (inlet TC, placed in the middle isothermal region of the furnace) and the other at the outlet of the reactor. The outlet flow was analysed throught a GSD 350 OnmiStar mass spectrometer from Pfiffer Vacuum. The pipeline connecting BTA and mass spectrometer was heated to T = 423 K to avoid condensation.

2.2. Synthesis of Zr_TFA_NH$_2$

Zirconium chloride [$ZrCl_4$, FW = 233.02 g mol^{-1}, 0.121 g, 0.52 mmol] and trifluoroacetic acid (1 mL) were mixed together and diluted with *N*,*N*-dimethylformamide (DMF, 25 mL). The resulting suspension was sonicated in an ultrasonic bath at ambient temperature for 15 minutes, this yielding a clear colorless solution. After that time, H_2BDC-NH_2 (FW = 181.15 g mol^{-1}, 0.050 g, 0.26 mmol, 0.5 equiv.) was added to the solution; the mixture was further diluted with fresh DMF (25 mL), sonicated for additional 15 minutes and finally transferred to a Teflon-lined stainless-steel autoclave (inner Teflon beaker volume *ca.* 100 mL). The autoclave was sealed and heated at T = 393 K for 72 h under autogenous pressure. After slow overnight cooling, the microcrystalline light yellow powder of **Zr_TFA_NH$_2$·DMF** was collected, washed with ethanol (3 × 10 mL) and petroleum ether (3 × 10 mL) and finally dried under a nitrogen stream at room temperature. Yield: 0.13 g {67%, based on the minimal formula $[Zr_6O_4(OH)_4(TFA)_{4.2}(BDC\text{-}NH_2)_{3.9}]\cdot 4(DMF)$}. Elemental analysis calcd. (%) for **Zr_TFA_NH$_2$·DMF**, $C_{51.6}H_{59.3}F_{12.6}N_{7.9}O_{35.5}Zr_6$ (MW = 2144.9 g mol^{-1}): C 28.9, H 2.8, N 5.2. Elemental analysis found (%): C, 29.0; H, 2.9; N, 5.1. IR bands (KBr pellet, cm^{-1}, Fig. S2): 1680(vs, sh) [ν(COO)$_{BDC\text{-}NH_2}$], 1657(vs) [ν(COO)$_{TFA}$], 1573(s) [ν(C=C)], 1507(w), 1437(vs), 1387(vs) [δ(C–H)], 1260(s) [ν(C–F)], 1204(s), 1145(m), 1101(m), 1024(w), 803(m), 770(m), 721(w) [γ(C–H)], 664(s), 567(w, br), 489(m, br).

2.3. Synthesis of Zr_TFA_PyPy

Zirconium chloride [$ZrCl_4$, FW = 233.02 g mol^{-1}, 0.124 g, 0.52 mmol] and trifluoroacetic acid (1 mL) were mixed together and diluted with *N*,*N*-dimethylformamide (DMF, 25 mL). The resulting suspension was sonicated in an ultrasonic bath at ambient temperature for 15 minutes, this yielding a clear colorless solution. After that time, H_2PyPy (FW = 244.20 g mol^{-1}, 0.063 g, 0.26 mmol, 0.5 equiv.) was added to the solution; the mixture was further diluted with fresh DMF (25 mL), sonicated for additional 15 minutes and finally transferred to a Teflon-lined stainless-steel autoclave (inner Teflon beaker volume *ca.* 100 mL). The autoclave was sealed and heated at T = 393 K for 72 h under autogenous pressure. After slow overnight cooling, the microcrystalline off-white powder of **Zr_TFA_PyPy·DMF** was collected, washed with ethanol (3 × 10 mL) and petroleum ether (3 × 10 mL) and finally dried under a nitrogen stream at room temperature. Yield: 0.11 g {58%, based on the minimal formula $[Zr_6O_4(OH)_4(TFA)_{1.8}(PyPy)_{5.1}]\cdot(DMF)$}. Elemental analysis calcd (%) for **Zr_TFA_PyPy·DMF**, $C_{67.8}H_{41.6}O_{33}N_{11.2}F_{5.4}Zr_6$ (MW = 2191.1 g mol^{-1}): C 37.2, H 1.9, N 7.2. Elemental analysis found (%): C, 37.4; H, 2.1; N, 7.3. IR bands (KBr pellet, cm^{-1}, Fig. S3): 1650(s, sh) [ν(COO)$_{PyPy}$], 1596(vs) [ν(COO)$_{TFA}$], 1555(m, sh) [ν(C=C)], 1419(vs) [δ(C–H)], 1248(w), 1206(w) [ν(C–F)], 1161(w), 1056(vw), 1028(w), 847(w, br), 779(m) [γ(C–H)], 654(m), 458(w).

2.4. Crystal structure analysis from PXRD data and DFT calculations

The PXRD patterns of **Zr_TFA_NH$_2$** and **Zr_TFA_PyPy** were indexed *ab initio* by using *N-TREOR* implemented in the *EXPO2014* program.[30] The best unit cell solutions found were $a = b = c = 20.7988$ Å and $\alpha = \beta = \gamma = 90^\circ$ for **Zr_TFA_NH$_2$** and $a = b = c = 26.3361$ Å and $\alpha = \beta = \gamma = 90^\circ$ for **Zr_TFA_PyPy**. The systematic extinction analysis suggested $Fm\bar{3}m$ as most probable space group for both MOFs, thus confirming the structural similarities with the already reported UiO-66-NH$_2$[31] and UiO-67-PyPy.[32] However, the presence of both HTFA/H$_2$BDC-NH$_2$ linkers for **Zr_TFA_NH$_2$** and HTFA/H$_2$PyPy linkers for **Zr_TFA_PyPy** (as assessed by ^{1}H NMR analysis of the digested sample) suggested a complete disordered linkers configuration into the MOF framework as required by the highly symmetric space group. An ordered linkers disposition would result in a less symmetric space group due to the symmetry lowering of the [Zr$_6$] nodes. A structural model was obtained starting from the crystal structures of UiO-66-NH$_2$ and UiO-67-PyPy. In **Zr_TFA_NH$_2$**, the crystal symmetry was reduced from $Fm\bar{3}m$ to $P\bar{4}3m$ in order to work with two independent linkers in the asymmetric unit; half of the BDC-NH$_2$$^{2-}$ molecule was replaced by one TFA$^-$, thus obtaining the minimal formula [Zr$_6$O$_4$(OH)$_4$(TFA)$_6$(BDC-NH$_2$)$_3$] which displays a higher TFA/BDC-NH$_2$ ratio than that of the experimental formula [Zr$_6$O$_4$(OH)$_4$(TFA)$_{4.2}$(BDC-NH$_2$)$_{3.9}$] (see SI). The same symmetry reduction was also carried out for **Zr_TFA_PyPy**. In this case, in order to reproduce to the experimental formula [Zr$_6$O$_4$(OH)$_4$(TFA)$_{1.8}$(PyPy)$_{5.1}$] only one third of the carboxylic PyPy^{2-} linkers were replaced by TFA$^-$ anions providing the minimal formula [Zr$_6$O$_4$(OH)$_4$(TFA)$_3$(PyPy)$_{4.5}$]. Due to the equivalent positions of the space group used, this was the only possibility to simulate as much as possible the real MOF composition as derived from the sample digestion followed by ^{1}H NMR analysis. The two structural models were then optimzed by DFT.

2.5. Textural properties assessment through N$_2$ adsorption. CO$_2$ and SF$_6$ adsorption isotherms

The powdered samples (*ca.* 40 mg) of **Zr_TFA_NH$_2$** and **Zr_TFA_PyPy** were activated at $T = 423$ K under high vacuum (10^{-6} torr) for 24 h before the measurement. The Brunauer–Emmett–Teller (BET) specific surface area, pore size distribution and pore volume (V_{tot}, V_{micro}) were estimated by volumetric adsorption with an ASAP 2020 Micromeritics instrument, using N$_2$ as adsorbate at $T = 77$ K. For the BET specific surface area calculation, the 0.01–0.1p/p_0 pressure range of the isotherm was used to fit the data. Within this range, all the Rouquerol consistency criteria[33,34] are satisfied (Fig. S4 and S5). The material (micro)porosity was determined from the N$_2$ adsorption isotherm using a NLDFT method (Tarazona approximation) and assuming a cylindrical pore shape (typical of metal oxides). CO$_2$ and SF$_6$ adsorption isotherms were recorded at $T = 273$ K, 298 K and 323 K at a maximum pressure of 1.2 bar. The isosteric heat of adsorption (Q_{st}) values of both gases were calculated from the three isotherms according to the differential form of the Clausius–Clapeyron equation:[35,36]

$$\left[\frac{\partial(\ln p)}{\partial\left(\frac{1}{T}\right)}\right]_\theta = -\frac{Q_{st}}{R} \quad (1)$$

where R is the gas constant (8.314 J K^{-1} mol^{-1}). The lowest comparable coverage of the two gases for the two MOFs is 0.4/0.2 wt% (CO$_2$) and 2.4/0.9 wt% (SF$_6$) for **Zr_TFA_NH$_2$**/**Zr_TFA_PyPy**, respectively. The IAST A/B adsorption selectivity (A, B = SF$_6$, CO$_2$, N$_2$) of binary mixtures at a total pressure of 0.5 bar (for the sake of comparison with the experimental data) and at $T = 298$ K was determined as the ratio of the adsorbed molar fractions of the two gases divided by the ratio of the gas phase initial molar fractions:[37]

$$S_{A/B} = \frac{\left(\frac{\chi_A}{\chi_B}\right)_{ads}}{\left(\frac{\chi_A}{\chi_B}\right)_{gas}} \quad (2)$$

The $(\chi_A)_{ads}$ and $(\chi_B)_{ads}$ values were derived from the application of the free software IAST++[38] to the experimental single-component isotherms collected at the chosen temperature. The initial composition (%) selected for the calculation was [50 : 50] for the [SF$_6$: CO$_2$] pair and [1 : 99] for the [G : N$_2$] pairs (G = SF$_6$, CO$_2$). Various models (Langmuir, Freundlich, BET, Henry, Dual-Site Langmuir–Freundlich) were employed for the SF$_6$, N$_2$ and CO$_2$ isotherms fitting, choosing the option that gives the lowest R^2 on the experimental points.

2.6. Breakthrough measurements

BT measurements were performed at a partial pressure of 0.25 of CO$_2$ and/or SF$_6$ in a carrier, at ambient temperature and pressure, under a constant flow of 10 mL min^{-1}. The samples were prepared by pelletizing the MOF powders at $p = 1$ ton and the pellets were sieved selecting the 250–500 μm size fraction. The bed packing density was 0.3 g mL^{-1}, with a resulting total porosity (ε_t) of 0.85. The bed porosity (ε_b) was instead estimated at 0.4 based on literature data.[39] For each sample, the sorption of CO$_2$ alone, SF$_6$ alone and the competitive sorption of CO$_2$ and SF$_6$ were performed. The partial pressure of 0.25 for each sorptive was chosen as the best compromise between the use of the carrier and the enhancement of BT times. The resulting 50 : 50 gas composition in the competitive BT measurements was chosen as a model to study the separation process. The total flow was set as low as possible to measure equilibrium data. The samples were pre-treated by heating at $T = 423$ K with a 5 K min^{-1} ramp under 25 mL min^{-1} He (99.9995%) flow for 24 h before the first experiment to allow full removal of DMF solvent. The same pre-treatment was performed before each subsequent experiment, but it was performed for 10 h, to allow full regeneration. The samples were then cooled down to room temperature under a 25 mL min^{-1} He flow. The procedure for each adsorption experiment foresees: (i) 10 min under 9.975 mL min^{-1} He and 0.025 mL min^{-1} of Ar (used as tracer), to equilibrate the mass baseline; in

the meantime, 2.500 mL min^{-1} CO_2 (99.998%) and/or 2.500 mL min^{-1} SF_6 (99.97%) were flowed to the by-pass to stabilize the flow; (ii) CO_2 and/or SF_6 gases are switched to reactor and contemporary He flow was reduced to keep the total volumetric flow constant at 10 mL min^{-1}. The adsorption was conducted until stabilization of the mass signal. Each adsorption experiment was followed by the desorption. The desorption was conducted by switching off CO_2 and/or SF_6 flows and contemporary increasing the He flow to keep the total volumetric flow constant at 10 mL min^{-1}. Blank experiments were performed on the empty reactor. For details of the calculations and for the schematic of the inlet flows please refer to the SI and Fig. S6.

2.7. Computational details

Periodic density functional theory (DFT) calculations were carried out at the PBEsol0-3c level of theory, as implemented in the *CRYSTAL23*[40] *ab initio* code. In the PBEsol0-3c method,[41,42] the total energy computed with the PBEsol0 hybrid functional combined with a double-ζ quality Gaussian basis set is augmented with two semi-empirical corrections to remove the basis set superposition error (BSSE) through the geometrical CounterPoise (gCP)[43] approach and to properly describe weak interactions *via* the D3 scheme[44] in its Becke–Johnson rational damping variant. A (75, 974) pruned grid was employed for the numerical evaluation of the exchange–correlation term, corresponding to the XLGRID keyword as used by the CRYSTAL code. Default convergence criteria for geometry optimization were employed, while the tolerances for one- and two-electron integrals calculation were set to 10^{-7}, 10^{-7} for the Coulomb and to 10^{-7}, 10^{-7}, 10^{-25} for the exchange series, respectively. The shrinking factors for the diagonalization of the Kohn–Sham matrix in the reciprocal space were set to 2 for the Monkhorst–Pack net and to 2 for the Gilat net. A full relaxation of both unit cell parameters and atomic positions was performed.

3. Results and discussion

3.1. Synthesis and characterization of Zr_TFA_NH_2 and Zr_TFA_PyPy

With the aim of preparing robust mixed-linker MOFs with both basic and fluorinated groups, we decided to focus on the zirconium MOFs of the UiO-6x family with cubic **fcu** topology as the best candidates because of their intrinsic chemical and thermal stability.[29] In particular, a "short" basic linker (to get an "UiO-66-like" MOF) and a "long" basic linker (to get an "UiO-67-like" MOF) were selected to build the MOFs to study the effect of the related different pore size on their adsorption/separation capability. Accordingly, the linkers of choice were the two commercially available 2-aminoterephtalic acid and [2,2′-bipyridine]-5,5′-dicarboxylic acid. On the other hand, the fluorinated part comes from the trifluoroacetic acid modulator added to the reaction mixture to improve the material crystallinity. Given the initial (defective) [Zr : linker] stoichiometric ratio (2 : 1 instead of 1 : 1 as normally required for the synthesis of defect-free UiO-6x MOFs),[29] the vacant coordination sites on the [Zr_6] octahedral node are filled by the modulator, thus giving a mixed-linker MOF with dual basic/fluorinated nature. A solvothermal synthesis carried out in DMF for three days and using dilute solutions directly provided the pure products. **Zr_TFA_NH_2** and **Zr_TFA_PyPy** have been thoroughly characterized in the solid state. The IR spectroscopic analysis confirms the presence of both linkers (Fig. S2 and S3), highlighting some typical bands of H_2BDC-NH_2/H_2PyPy at 1680/1651 cm^{-1} [ν(COO)], 1573/1555 cm^{-1} [ν(C=C)], 1387/1419 cm^{-1} [δ(C–H)], and 721/779 [γ(C–H)] respectively, besides those of TFA^- at 1657/1596 cm^{-1} [ν(COO)] and at 1260/1206 cm^{-1} [ν(C–F)].[45,46] In order to investigate the main elements present in the samples and their morphological homogeneity, SEM-EDX analysis was performed (Fig. S7 and S8). Both MOFs are in the form of uniform polyhedric microcrystals typical of a unique phase, organized in dense aggregates. Besides carbon and oxygen, EDX analysis confirmed the presence of zirconium, fluorine and nitrogen. Powder X-ray diffraction (PXRD, Fig. 1a) confirms that

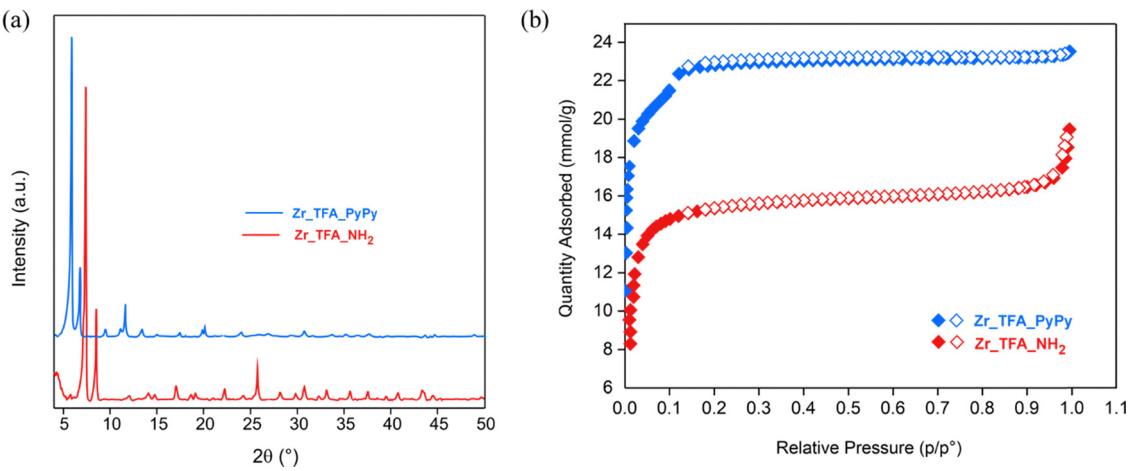

Fig. 1 (a) PXRD patterns (4–50° 2θ region) of **Zr_TFA_NH_2** and **Zr_TFA_PyPy** at comparison. (b) N_2 isotherms measured at T = 77 K on thermally activated **Zr_TFA_NH_2** and **Zr_TFA_PyPy** at comparison. Empty symbols denote the desorption branch.

the products have the same crystallographic symmetry (cubic, space group $Fm\bar{3}$ or $Fm\bar{3}m$) as those of UiO-66-NH_2[31] and UiO-67-PyPy.[32,47] The relative amount of fluorinated and non-fluorinated linkers in each MOF was quantified through ^{1}H and ^{19}F NMR spectroscopy *via* relative integration of selected ^{1}H and ^{19}F NMR signals in **Zr_TFA_NH$_2$** and **Zr_TFA_PyPy** solutions with respect to those of the standard solution (see Experimental section and SI). Consequently, based on the ligands relative stoichiometric ratio the MOFs minimal formulae can be written as $[Zr_6O_4(OH)_4(TFA)_{4.2}(BDC\text{-}NH_2)_{3.9}]$ and $[Zr_6O_4(OH)_4(TFA)_{1.8}(PyPy)_{5.1}]$. Thermogravimetric analysis (TGA, Fig. S9a and S10a) showed that the thermal stability of both MIXMOFs is lower than that of their non-defective parent materials UiO-66-NH_2 (T_{dec} = 823 K)[31] or Zr_PyPy (T_{dec} = 800 K)[32] (T_{dec} = 800/783 K for **Zr_TFA_NH$_2$**/**Zr_TFA_PyPy**, respectively). This is caused by the lower node connectivity (presence of defects) in our samples. In **Zr_TFA_NH$_2$**, an initial weight loss of *ca.* 14 wt% can be reasonably ascribed to loss of clathrated DMF coming from the synthesis (theoretical mass loss = 13.6 wt%). The DTG peak found in this range falls at T = 470 K. Further proof of evidence is provided by the MS analysis of the volatiles (Fig. S9b), where the peak at m/z = 73 a.m.u. typical of DMF appears in the same temperature range. Subsequently, another loss of *ca.* 20 wt% centered at T = 615 K is ascribed to TFA (m/z = 45 a.m.u. on the MS spectrum; theoretical mass loss = 21 wt%) before undergoing final decomposition at T_{dec}. In **Zr_TFA_PyPy**, the visible thermal events are a first clathrated DMF solvent loss (*ca.* 4 wt%; theoretical mass

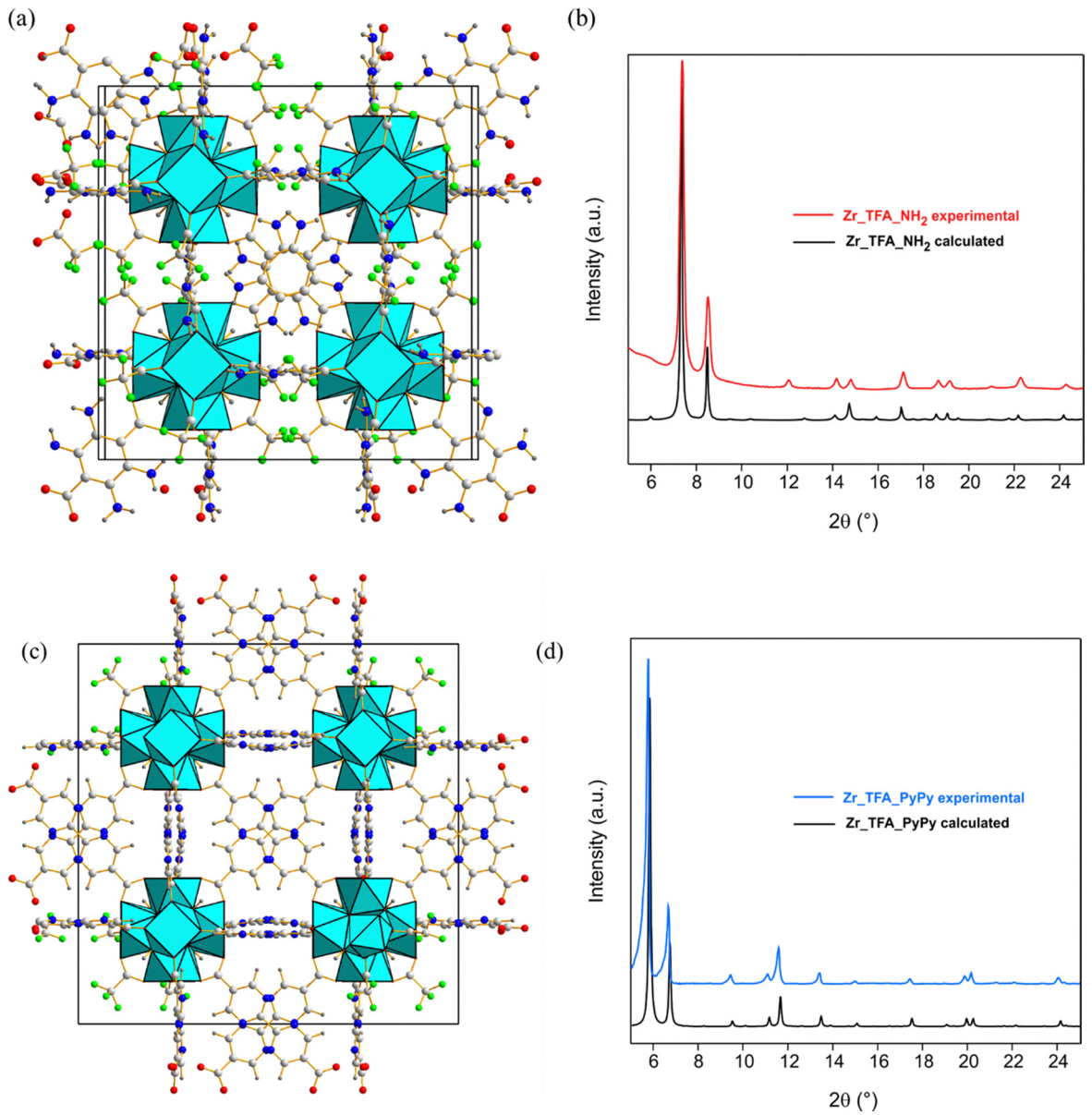

Fig. 2 Polyhedral representation of **Zr_TFA_NH$_2$** (a) and **Zr_TFA_PyPy** (c) viewed along the *c*-axis. Comparison between the calculated and experimental patterns (b) and (d). atom color code: Zr turquoise, O red, C grey, H white, F green and N blue.

loss = 3.3 wt%) centered at T = 473 K (m/z = 73 a.m.u. in the mass spectrum of the volatiles, Fig. S10b) and the final MOF decomposition at T_{dec} witnessed by the presence in the MS spectrum of the peak at m/z = 79 a.m.u. related to pyridine (coming from H_2PyPy degradation).

3.2. Crystal structure description

The structure of the two MIXMOFs as obtained by DFT calculations are shown in Fig. 2a–c, whereas comparison between the calculated and experimental patterns are shown in Fig. 2b–d.

The two DFT models provide a good agreement between the calculated and observed patterns. The generated CIF files are available as SI. However, they were not validated through Rietveld refinement because of the high number of free parameters to refine against the low number of reflections that imposed strong restraints and caused instability in the convergence procedure. As already mentioned in the Experimental section, to describe the presence of the two linkers in the right stoichiometry a symmetry reduction from the F-centred high symmetry $Fm\bar{3}m$ cubic space group to the less symmetric primitive $P\bar{4}3m$ group has been made. This allowed to handle the two linkers in the asymmetric unit independently, building a reliable structural model for both MOFs. However, the systematic extinction analysis of the diffraction patterns suggested the conventional **fcu** structure with $Fm\bar{3}m$ as space group. This means that for a mixed-linker system their real disposition around the [Zr_6] clusters is completely disordered, giving rise to statistically equivalent reticular nodes. Obviously, our models generated instead *ordered* SBUs made of [Zr_6] clusters with different chemical envinroments. The hexanuclear clusters for the two MOFs are reported in Fig. 3.

The $[Zr_6O_4(OH)_4]^{12+}$ hexanuclear cluster for **Zr_TFA_NH$_2$** is charge-compensated by six apical bridging BDC-NH_2^{2-} linkers and six TFA^- anions all placed in the equatorial region. Given the monovalent nature of TFA^-, in the proposed crystal structure there is an excess of this linker with respect to the equimolar composition found by NMR experiments. As for **Zr_TFA_PyPy**, the charges are compensated by nine bridging $PyPy^{2-}$ linkers and three adjacent TFA^- anions thus giving the overall minimal formula (taking into account the bivalent nature of $PyPy^{2-}$ and monovalent nature of TFA^-) $[Zr_6O_4(OH)_4(TFA)_3(PyPy)_{4.5}]$ as best match with the experimentally found $[Zr_6O_4(OH)_4(TFA)_{1.8}(PyPy)_{5.1}]$. Overall, the calculated patterns of both MOFs here modelled display good agreement with the experimental ones. We believe that our models represent the best compromise to describe a mixed-linker fully disordered structure in a highly symmetric space group maintining the right stoichiometry.

3.3. Textural properties assessment. CO_2 and SF_6 adsorption isotherms

The porosity of **Zr_TFA_NH$_2$** and **Zr_TFA_PyPy** was evaluated through volumetric N_2 adsorption at T = 77 K on pre-activated samples (Fig. 1b). The isotherm shape is of Type I, typical of

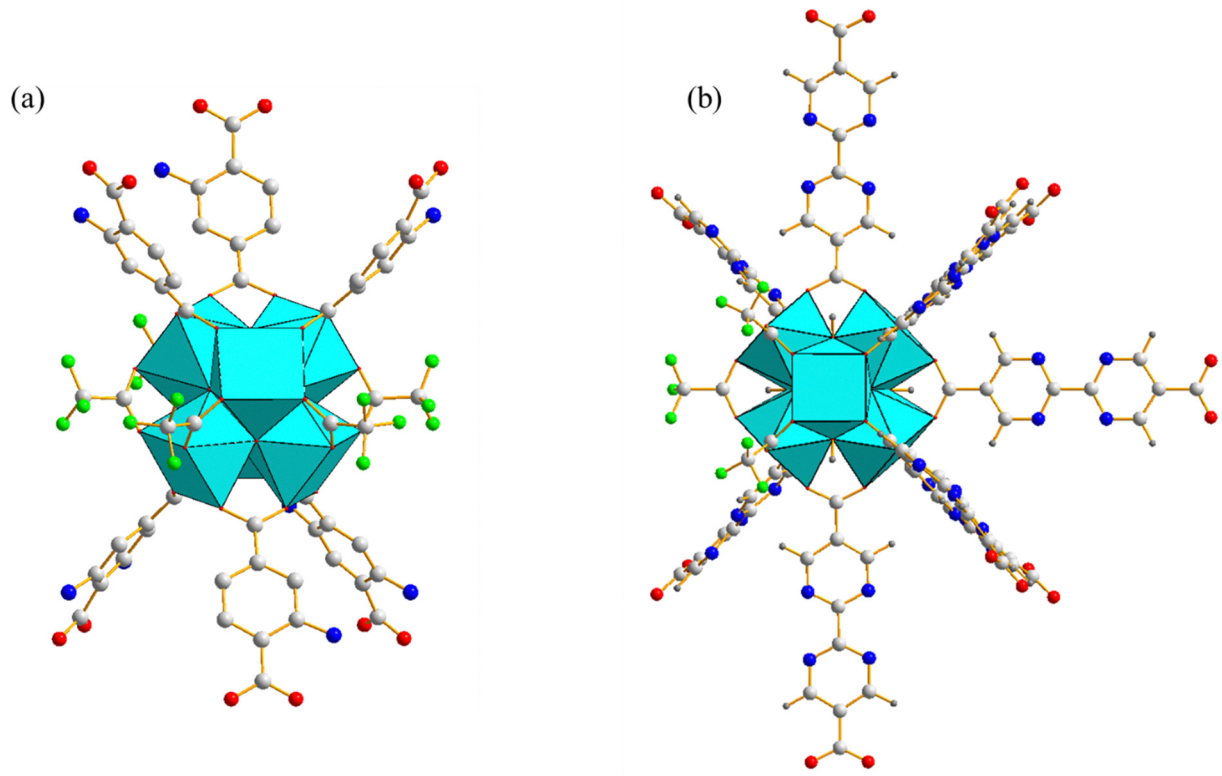

Fig. 3 Details of the connectivity of the [Zr_6] clusters in **Zr_TFA_NH$_2$** (a) and **Zr_TFA_PyPy** (b). The $PyPy^{2-}$ moiety is represented as disordered in two equivalent 180° tilted positions. Atom color code: Zr turquoise, O red, C grey, H white, F green and N blue.

microporous materials. The measured BET surface areas are 1380 and 1922 $m^2\ g^{-1}$ for **Zr_TFA_NH$_2$** and **Zr_TFA_PyPy**, respectively. The accessible surface areas were also estimated through the Mercury crystallographic software[48] starting from the CIF files generated after DFT optimization and using N_2 as probe. The calculated values are 1100 and 2200 $m^2\ g^{-1}$, respectively. While in **Zr_TFA_NH$_2$** the accessible surface area is higher than that of its parent MOF UiO-66-NH_2 (BET area = 1112 $m^2\ g^{-1}$),[31] in **Zr_TFA_PyPy** the opposite trend is observed in comparison with the non-defective analogue Zr_PyPy (BET area = 2730 $m^2\ g^{-1}$).[32] The total pore volume equals 0.54 and 0.81 $cm^3\ g^{-1}$ for **Zr_TFA_NH$_2$** and **Zr_TFA_PyPy**, respectively. The DFT micropore size distribution (Fig. S11) shows a comparable pore size at $15 \leq w \leq 19$ Å, with an additional contribution at $w \approx 23$ Å for **Zr_TFA_PyPy** that is absent in **Zr_TFA_NH$_2$**. The activated materials have been tested in CO_2 and SF_6 adsorption at p_{max} = 1.2 bar and at variable temperatures: T = 273, 298 and 323 K. Fig. 4a and b report the ambient temperature CO_2 and SF_6 isotherms for both MOFs, respectively. The CO_2 uptake at p_{CO_2} = 1 bar and T = 298 K is 7.6 wt% (1.7 mmol g^{-1}) and 7.2 wt% (1.6 mmol g^{-1}) for **Zr_TFA_NH$_2$** and **Zr_TFA_PyPy**, respectively. The efficiency of the amino group in capturing CO_2 is higher than that of pyridine, given the higher amount adsorbed by the former despite its lower surface area. This may be due to the ability of the $-NH_2$ group at reacting with CO_2 (reversibly) to form carbamates.[12,13] In line with this statement, the amount of CO_2 adsorbed at ambient temperature and pressure by **Zr_TFA_NH$_2$** is lower than that adsorbed by the non-defective analogue UiO-66-NH_2 (3.04 mmol g^{-1})[49] and similar to that of UiO-66 (2.0 mmol g^{-1}).[49] The amount of CO_2 adsorbed by **Zr_TFA_PyPy** is comparable to that of its defect-free analogue Zr_PyPy (1.5 mmol g^{-1})[50] and higher than that of UiO-67 (1.2 mmol g^{-1}).[51] A much better improvement of the materials CO_2 thermodynamic affinity is observed for both mixed-linker MOFs in comparison with their homo-linker analogues in the CO_2 isosteric heat of adsorption at zero coverage (Q_{st}) values. Q_{st} has been calculated from the isotherms collected at three different temperatures applying the Clausius–Clapeyron equation. The values of 29 and 28 kJ mol^{-1} for **Zr_TFA_NH$_2$** and **Zr_TFA_PyPy** respectively outperform those reported for UiO-66-NH_2 (25 kJ mol^{-1})[49] and Zr_PyPy (21 kJ mol^{-1}),[50] proving the beneficial effect of the simultaneous presence of the basic and fluorine-containing linkers on carbon dioxide adsorption. As for SF_6, the uptake at p_{SF_6} = 1 bar and T = 298 K is 21.6 wt% (1.5 mmol g^{-1}) and 34.5 wt% (2.4 mmol g^{-1}) for **Zr_TFA_NH$_2$** and **Zr_TFA_PyPy**, respectively. The absolute gas uptake at ambient temperature is proportional to the material surface area and it is much higher than that found for other Zr-based MOFs from the literature with smaller pore size like UiO-66-Br_2 (0.9 mmol g^{-1}),[52] but it is lower than that of UiO-67 (4.0 mmol g^{-1}).[53] In terms of SF_6 isosteric heat of adsorption at zero coverage (Q_{st}), the mixed-linker MOFs are featured by a comparable Q_{st} value than those found for their homo-linker parent analogues: 31 *vs.* 32 or 33 kJ mol^{-1} for **Zr_TFA_NH$_2$** *vs.* UiO-66-NH_2[52] or UiO-66,[54] respectively; 23 *vs.* 20 kJ mol^{-1} for **Zr_TFA_PyPy** *vs.* UiO-67,[53] respectively (Table 1 and Table S1). This indicates that the simultaneous presence of a basic and a fluorinated linker in the material does not increase its SF_6 thermodynamic affinity significantly, while it has a more important effect for CO_2. Interestingly, the variation of the MOFs pore size when passing from a "short" amino-terephthalate to a "long" bipyridyl linker induces a switch in the thermodynamic affinity for the two gases: while in **Zr_TFA_NH$_2$** $Q_{st}(SF_6) > Q_{st}(CO_2)$, the opposite holds for **Zr_TFA_PyPy**, where $Q_{st}(CO_2) > Q_{st}(SF_6)$. Therefore, these MOFs may represent useful materials for the discrimination of these polluting gases, opening new horizons in the field of air treatment and cleaning. To shed further light on the MOFs adsorption behavior, IAST selectivity (S_{SF_6/CO_2}) data for [SF_6/CO_2] binary equimolar mixtures at T = 298 K were estimated; the results are summarized in Table 2. Both MOFs are selective towards SF_6, but **Zr_TFA_NH$_2$** is a better-performing material than **Zr_TFA_PyPy**. The presence of N_2 in the real atmospheric composition does not interfere with the separation process, since both MOFs are selective for SF_6 or CO_2 over N_2 even at very diluted greenhouse gas concentration, as inferred from the N_2 isotherms recorded at T = 298 K (Fig. S12) and related S_{SF_6/N_2} and S_{CO_2/N_2} IAST selectivity values estimated on a binary [G : N_2] [1 : 99] mixture (G = SF_6, CO_2).

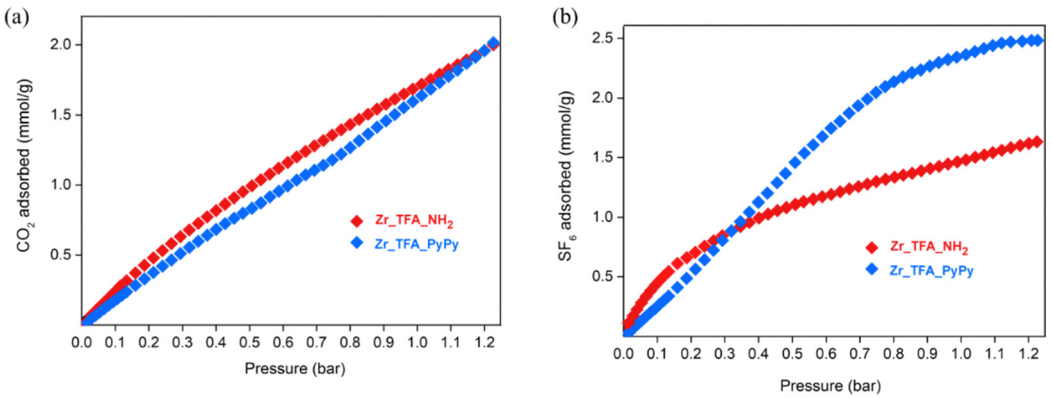

Fig. 4 Collective (a) CO_2 and (b) SF_6 adsorption isotherms at T = 298 K for **Zr_TFA_NH$_2$** and **Zr_TFA_PyPy** at comparison.

Table 1 Main adsorption data for the MOFs in this study

Sample	BET area [$m^2\ g^{-1}$]	Q_{st} (CO_2) [kJ mol^{-1}]	CO_2 quantity adsorbed at T = 298 K, p = 1 bar [mmol g^{-1}]	Q_{st} (SF_6) [kJ mol^{-1}]	SF_6 quantity adsorbed at T = 298 K, p = 1 bar [mmol g^{-1}]
Zr_TFA_NH$_2$	1380	29	1.7 (7.6 wt%)	31	1.5 (21.6 wt%)
Zr_TFA_PyPy	1922	28	1.6 (7.2 wt%)	23	2.4 (34.5 wt%)

Table 2 IAST SF_6/CO_2, SF_6/N_2 and CO_2/N_2 adsorption selectivity data of binary gas mixtures [50 : 50] or [1 : 99] at p_{tot} = 0.5 bar and T = 298 K for **Zr_TFA_NH$_2$** and **Zr_TFA_PyPy**

MOF	S_{SF_6/CO_2} [50 : 50]	S_{SF_6/N_2} [1 : 99]	S_{CO_2/N_2} [1 : 99]
Zr_TFA_NH$_2$	1.8	5.4	2.4
Zr_TFA_PyPy	1.5	3.2	2.4

3.3. Breakthrough experiments with SF_6/CO_2 mixtures

To go deeper in studying the performances of **Zr_TFA_NH$_2$** and **Zr_TFA_PyPy** in the CO_2/SF_6 competitive sorption, the breakthrough (BT) curves were recorded and the amount adsorbed in dynamic measurements was calculated. The BT adsorption curves of the single pure gases recorded on **Zr_TFA_NH$_2$** (Fig. 5a, empty symbols) show that the retention time of SF_6 is longer than that of CO_2 ($\approx$2 and $\approx$1 dimensionless time, respectively. The dimensionless time was calculated by normalization of experimental time by the retention time of an inert gas). The BT curves were recorded under the closest conditions to equilibrium as possible. This was achieved through the adoption of a very low total flow rate and the use of He as inert carrier, that favors molecular diffusivity.[55] Knudsen diffusion was favored by adequate sample preparation (pelletizing and sieving the pellets in the fraction 250–500 μm). This excludes major effects of external mass transfer resistance on the BT measurements.[55] Upon competitive adsorption (Fig. 5a, full symbols), the retention time of CO_2 is not affected at all, while that of SF_6 is substantially reduced to $\approx$1.3. This is reflected in the amount of adsorbed gas (Table 3): the amount of adsorbed

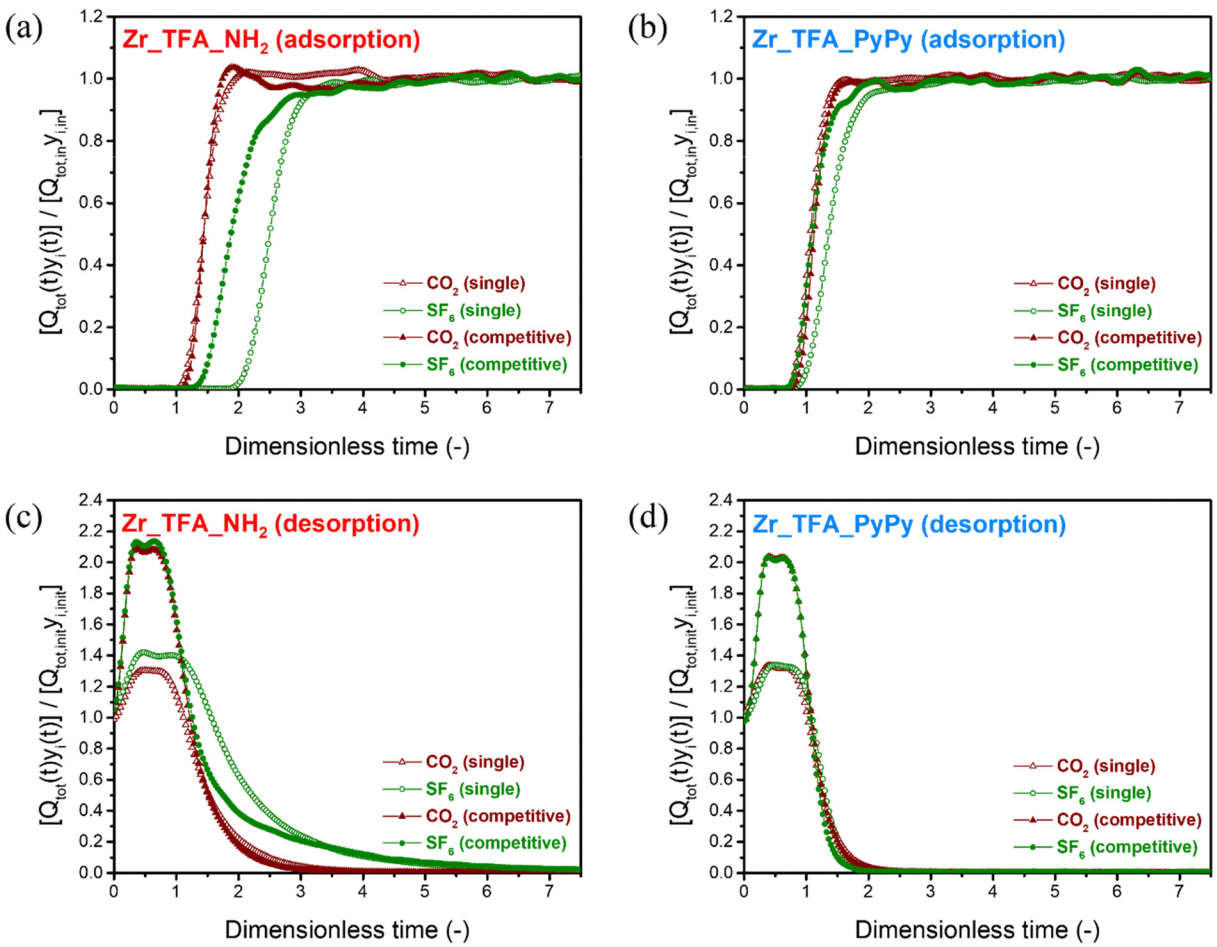

Fig. 5 Breakthrough curves of adsorption (a) and (b) and desorption (c) and (d) experiments on **Zr_TFA_NH$_2$** and **Zr_TFA_PyPy**.

Table 3 Amount of CO_2 and SF_6 adsorbed in breakthrough experiments (namely under dynamic conditions) on **Zr_TFA_NH$_2$** and **Zr_TFA_PyPy**. In brackets the equilibrium data at $0.24p/p_0$ (from the adsorption isotherms of CO_2 and SF_6) are reported. The selectivity data are calculated at 0.5 of absolute pressure in a 1 : 1 : 2 mixture of CO_2 : SF_6 : inert

	CO_2 adsorbed, single [mmol g^{-1}]	SF_6 adsorbed, single [mmol g^{-1}]	CO_2 adsorbed, competitive [mmol g^{-1}]	SF_6 adsorbed, competitive [mmol g^{-1}]	S_{SF_6/CO_2}
Zr_TFA_NH$_2$	0.30 (0.53)	0.75 (0.76)	0.35	0.63	1.8
Zr_TFA_PyPy	0.36 (0.42)	0.45 (0.64)	0.41	0.36	0.9

CO_2 slightly changes, in a range within the experimental error (0.30 and 0.35 mmol g^{-1} upon single and competitive adsorption, respectively), while that of SF_6 is significantly reduced (0.75 and 0.63 mmol g^{-1} upon single and competitive adsorption, respectively). This behavior gives some information about the adsorption sites for the two molecules. The amount of SF_6 adsorbed in single component experiment under dynamic conditions nicely fits with the value recorded in static conditions (SF_6 adsorption isotherm). On the contrary, the amount of adsorbed CO_2 is lower in dynamic than in static conditions. Moreover, the fact that the CO_2 adsorbed amount in dynamic single and competitive adsorption does not significantly change suggests that SF_6 does not compete with CO_2, but CO_2 partially competes with SF_6. A slight overshoot is present in the CO_2 BT adsorption curve, suggesting that, even if CO_2 could compete, upon arrival of the slowest SF_6 some CO_2 molecules are replaced by SF_6. This is also coherent with the $Q_{st}(SF_6)$ value higher than $Q_{st}(CO_2)$. Likewise, upon desorption (Fig. 5c) the effect of the higher $Q_{st}(SF_6)$ is visible in its broad desorption curve. The BT curves of the single gases on **Zr_TFA_PyPy** (Fig. 5b and d) show that the CO_2 retention time is not affected by the single-component or double-component adsorption, as observed in **Zr_TFA_NH$_2$**. On the other hand, SF_6 retention time is slightly reduced by the competition. Hence, the amount of CO_2 adsorbed does not significantly change going from single to competitive adsorption (0.36 and 0.41 mmol g^{-1} respectively) while the amount of SF_6 adsorbed is decreased from 0.45 to 0.36 mmol g^{-1}. Upon desorption, the SF_6 curve is slightly sharper than that of CO_2. To find an explanation for this behavior, the enlargement of the adsorption isotherms in the 0–0.26 bar range is reported in Fig. S13. Here, the straight lines highlight that at low relative pressure the SF_6 isotherm on **Zr_TFA_PyPy** is of type III, based on IUPAC classification (the isotherm turns to a Langmuir-like type I shape at higher pressures). This implies that the adsorption branch in the dynamic experiment is broader than the desorption branch. The SF_6 type III behavior on **Zr_TFA_PyPy** is also coherent with the low $Q_{st}(SF_6)$ of 23 kJ mol^{-1}. The opposite occurs for SF_6 on **Zr_TFA_NH$_2$**, where the Langmuir behavior of the isotherm at low relative pressure is strong: the adsorption branch is very sharp and the desorption branch is broad in dynamic experiments. The SF_6/CO_2 selectivity measured at 0.5 of partial pressure for the two samples shows an analogous trend as the calculated IAST selectivity at p_{tot} = 0.5 bar. In comparative terms, both experimental and calculated evicence highlight that **Zr_TFA_NH$_2$** is better than **Zr_TFA_PyPy** to achieve an efficient SF_6/CO_2 separation.

3.4. DFT analysis of the interaction of Zr_TFA_NH$_2$ and Zr_TFA_PyPy with CO_2 and SF_6

To cast light on the **Zr_TFA_NH$_2$** and **Zr_TFA_PyPy** adsorption sites, we modelled the interaction of CO_2 and SF_6 in the pores of the microporous materials using the complementarity of the electrostatic potential map (EPM), shown in Fig. S14 for both hosts and guests. A closer look at the MOFs highlights electrophilic (blue, positive) regions located around the $[Zr_6O_4(OH)_4]^{12+}$ moiety of the Inorganic Building Unit (IBU) and nucleophilic (red, negative) spots represented by the nitrogen atoms of the functionalised BDC-NH_2^{2-} and $PyPy^{2-}$ organic linkers and carboxylate/TFA^- groups on the octahedral metallic nodes. The PBEsol0-3c results for the adsorption of SF_6 and CO_2 on **Zr_TFA_NH$_2$** and **Zr_TFA_PyPy** are listed in Table S2 and S3 in the SI. For **Zr_TFA_NH$_2$**, the predicted adsorption energies are in good agreement with the experimental heats of adsorption (Q_{st}). For SF_6, the strongest binding site is located at the μ_3-OH groups of the MOF IBU (Fig. 6) through an O–H$\cdots$F–S hydrogen bond with a ΔE of -37.05 kJ mol^{-1} (*vs.* experimental Q_{st} = 31 kJ mol^{-1}); additional weak $\pi\cdots$F–S short contacts between the aromatic π cloud of BDC-NH_2^{2-} and SF_6 are present, together with S–F$\cdots$F–C interactions between SF_6 and the CF_3 group of TFA^-. For CO_2, the primary adsorption

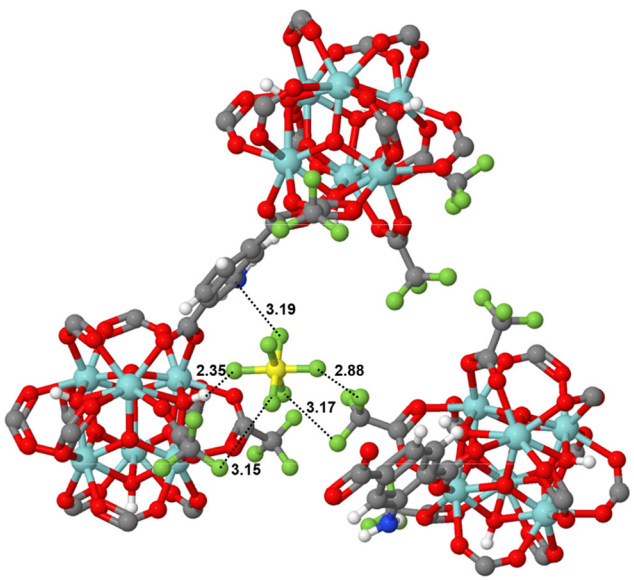

Fig. 6 Portion of the optimized PBEsol-03c geometry for [SF_6@**Zr_TFA_NH$_2$**] in the preferential adsorption site. The main gas-framework distances (Å) are reported. Atom color code: Zr turquoise, O red, C grey, H white, N blue, S yellow and F green.

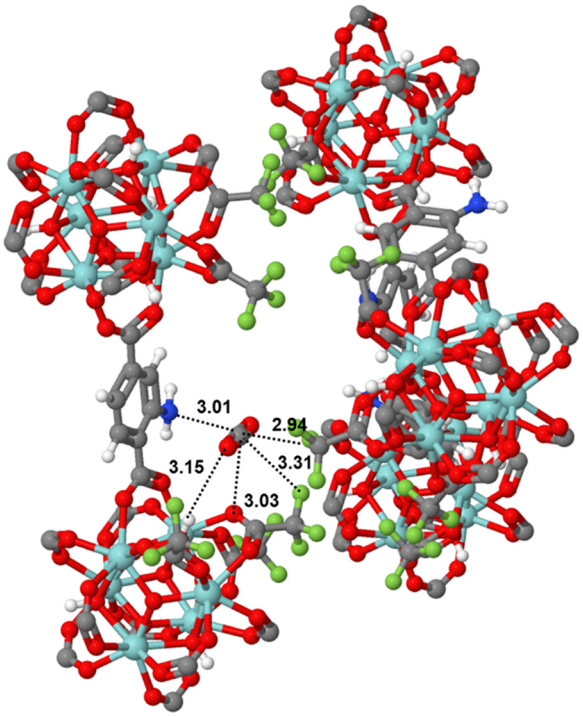

Fig. 7 Portion of the optimized PBEsol0-3c geometry for [CO_2@**Zr_T-FA_NH$_2$**]. The main gas-framework distances (Å) are reported. Atom color code: Zr turquoise, O red, C grey, H white and N blue.

site is represented by the functionalized BDC-NH_2^{2-} linker (Fig. 7) where the basic –NH_2 tag interacts with the acidic carbon atom of carbon dioxide providing a binding energy of −33.22 kJ mol^{-1} (*vs.* the experimental Q_{st} of 29 kJ mol^{-1}). Additional multiple weak interactions of both O═C═O···H–O and O_2C···F–C(TFA$^-$) type are also at work. In **Zr_TFA_PyPy**, SF_6 has the same binding sites as those observed in **Zr_TFA_NH$_2$**, the main being again the μ_3-OH groups of the MOF IBU (Fig. 8). CO_2 interacts *via* its quadrupole with $PyPy^{2-}$

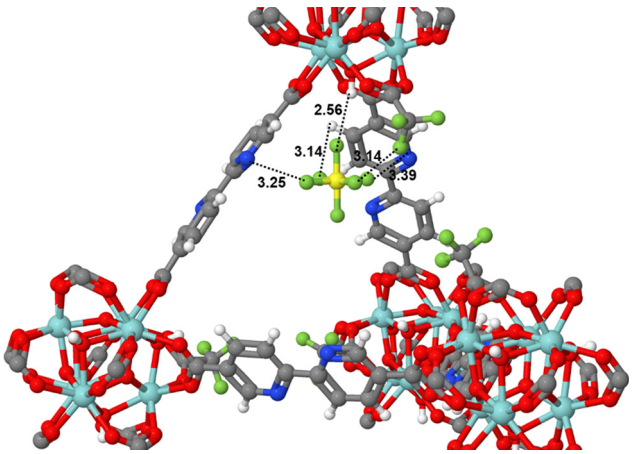

Fig. 8 Portion of the optimized PBEsol0-3c geometry for [SF_6@**Zr_TFA_-PyPy**]. The main gas-framework distances (Å) are reported. Atom color code: Zr turquoise, O red, C grey, H white, N blue, S yellow and F green.

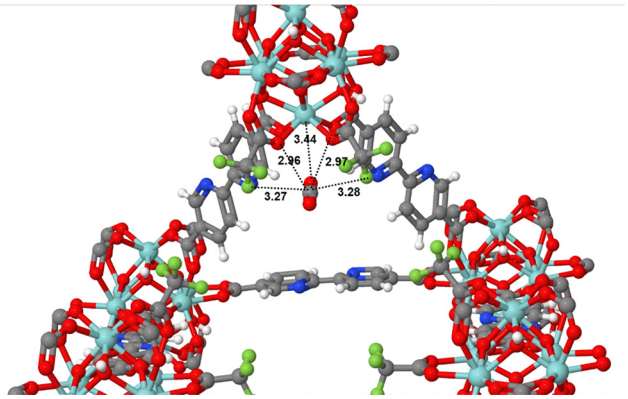

Fig. 9 Portion of the optimized PBEsol0-3c geometry for [CO_2@**Zr_T-FA_PyPy**]. The main gas-framework distances (Å) are reported. Atom color code: Zr turquoise, O red, C grey, H white and N blue.

carboxylates, polarized by the presence of the strongly electron-withdrawing CF_3 groups on TFA^-. Additional O═C═O···H–O and O_2C···F–C(TFA^-) contacts are found (Fig. 9). The calculated adsorption energies are −25.64 kJ mol^{-1} for SF_6 (*vs.* an experimental Q_{st} equal to 23 kJ mol^{-1}) and −26.98 kJ mol^{-1} for CO_2 (*vs.* an experimental Q_{st} of 28 kJ mol^{-1}). The interaction with the inorganic unit and the Zr atom is not site-specific; rather, it is averaged out by the surrounding atoms. CO_2 occupies a more favourable location within a pocket where quadrupolar interactions occur, as shown in Fig. 9. Although the specific role of the TFA^- groups cannot be identified, they do contribute overall to the binding of the molecules due to the formation of short contacts with the fluorine atoms.

Conclusions

This work demonstrates that combining basic and fluorinated linkers in the mixed-linker zirconium MOFs **Zr_TFA_NH$_2$** and **Zr_TFA_PyPy** effectively tunes their gas adsorption and separation behaviour towards CO_2 and SF_6. The dual functionalization strategy yields materials that display enhanced thermodynamic affinity for CO_2 compared to single-linker analogues. In addition, selective adsorption of SF_6 over CO_2 can be achieved in the smaller-pore **Zr_TFA_NH$_2$**, as confirmed by the dynamic breakthrough experiments. DFT analysis provided a molecular-level understanding of how pore size and functional group distribution govern adsorption energetics and selectivity. The results highlight the potential of these materials as scalable (given the commercial availability of their constituting linkers) adsorbents for discriminating between gases of different polarity and size, relevant to environmental applications such as capture of greenhouse gases from flue gases or industrial processes or separation of gas mixtures in energy-efficient processes. Future development currently undergoing in our labs will include further tuning of MIXMOFs pore environment to target specific gas pairs of environmental concern.

Author contributions

G. P., G. B., C. Z., F. C., F. R., F. B.: investigation, formal analysis; B. C., G. G., G. T.: validation; L. D.: investigation, formal analysis, methodology, software, writing – original draft; A. R.: conceptualization, funding acquisition, project administration, supervision, writing – original draft.

Conflicts of interest

The authors have no conflicts of interest to declare.

Data availability

The data supporting this article have been included as part of the supplementary information (SI). Supplementary information: quantitative ^{1}H- and ^{19}F-NMR spectroscopy on the digested samples, additional characterization data (IR spectra, details of the BT calculations, FE-SEM images and related EDX analysis, TG-DTG-MS traces, micropore size distribution) and computational details (electrostatic potential maps). Comparative tables of SF_6 and CO_2 adsorption performance and of calculated interaction energies *vs.* experimental isosteric heats of adsorption. See DOI: https://doi.org/10.1039/d6ma00018e.

Acknowledgements

A. R. G. P. and G. B. would like to acknowledge the Italian Ministry of University and Research (MUR) and the European Union (Next Generation EU) for funding this research activity through the PRIN 2022 project LUMIMOF (2022A3XNWJ) ''Wastewater treatment and monitoring with luminescent mixed-linker Metal–Organic Frameworks as chemical sensors and adsorbents of contaminants of emerging concern''. This research was also funded by the European Union – NextGeneration EU from the Italian Ministry of Environment and Energy Security POR H2 AdP MMES/ENEA with involvement of CNR and RSE, PNRR – Mission 2, Component 2, Investment 3.5 ''Ricerca e sviluppo sull'idrogeno'', CUP: B93C22000630006. L. D., B. C, F. B. and F. R. acknowledge support from the ProjectCH4.0 under the MUR program ''Dipartimenti di Eccellenza 2023–2027'' (CUP: D13C22003520001) and the NODES project fundedby the European Union – NextGenerationEU, Mission 4 Component 1.5 – ECS00000036 – CUP D17G2200015000. C. Z. thanks the ''FASTTO0'' project (CUP J93C22000330006), funded through the Italian Ministry of Environment and Energy Security and the Circular and Sustainable Made in Italy Extended Partnership (MICS) funded by the European Union Next-Generation EU (Piano Nazionale di Ripresa e Resilienza (PNRR) – Missione 4, Componente 2, Investimento 1.3 – D.D. 1551.11-10-2022, PE00000004) for financial support.

References

1 https://unfccc.int/cop30 (last access: February 2026).
2 https://www.epa.gov/ghgemissions/carbon-dioxide-emissions (last access: February 2026).
3 https://www.epa.gov/ghgemissions/fluorinated-gas-emissions (last access: February 2026).
4 https://www.nobelprize.org/prizes/chemistry/2025/summary/ (last access: Febraury 2026).
5 O. M. Yaghi, M. J. Kalmutzki and C. S. Diercks, *Introduction to Reticular Chemistry: Metal-Organic Frameworks and Covalent Organic Frameworks*, Wiley-VCH Verlag GmbH & Co. KGaA, 2019.
6 H. García and S. Navalón, *Metal-Organic Frameworks: Applications in Separations and Catalysis*, ed. H. García and S. Navalón, Wiley-VCH Verlag GmbH Wiley-VCH Verlag GmbH & Co. KGaA, 2018.
7 S. Kaskel, *The Chemistry of Metal–Organic Frameworks: Synthesis, Characterization, and Applications*, ed. S. Kaskel, Wiley-VCH Verlag GmbH & Co. KGaA, 2016.
8 D. Farrusseng, *Metal-Organic Frameworks: Applications from Catalysis to Gas Storage*, Wiley-VCH Verlag, Weinheim, 2011.
9 M. Pugliesi, M. Cavallo, C. Atzori, B. Garetto, E. Borfecchia, L. Donà, B. Civalleri, G. Tuci, G. Giambastiani, S. Galli, F. Bonino and A. Rossin, *Adv. Funct. Mater.*, 2024, **34**, 2403017.
10 P. Campitelli, A. Tombesi, C. Di Nicola, C. Pettinari, A. Mauri, S. Galli, T. Yan, D. Liu, J. D. Duan, S. Goswami, G. Tuci, G. Giambastiani, J. T. Hupp and A. Rossin, *ACS Appl. Energy Mater.*, 2023, **6**, 9231–9242.
11 G. Mercuri, M. Moroni, S. Galli, G. Tuci, G. Giambastiani, T. Yan, D. Liu and A. Rossin, *ACS Appl. Mater. Interfaces*, 2021, **13**, 58982–58993.
12 G. Mercuri, M. Moroni, K. V. Domasevitch, C. Di Nicola, P. Campitelli, C. Pettinari, G. Giambastiani, S. Galli and A. Rossin, *Chem. – Eur. J.*, 2021, **27**, 4746–4754.
13 R. Vismara, G. Tuci, N. Mosca, K. V. Domasevitch, C. Di Nicola, C. Pettinari, G. Giambastiani, S. Galli and A. Rossin, *Inorg. Chem. Front.*, 2019, **6**, 533–545.
14 D. Morelli Venturi and F. Costantino, *RSC Adv.*, 2023, **13**, 29215–29230.
15 D. M. Venturi, M. S. Notari, R. Bondi, E. Mosconi, W. Kaiser, G. Mercuri, G. Giambastiani, A. Rossin, M. Taddei and F. Costantino, *ACS Appl. Mater. Interfaces*, 2022, **14**, 40801–40811.
16 A. Ebadi Amooghin, H. Sanaeepur, R. Luque, H. Garcia and B. Chen, *Chem. Soc. Rev.*, 2022, **51**, 7427–7508.
17 P. A. Sáenz Cavazos, M. L. Díaz-Ramírez, E. Hunter-Sellars, S. R. McIntyre, E. Lima, I. A. Ibarra and D. R. Williams, *RSC Adv.*, 2021, **11**, 13304–13310.
18 Y. W. Abraha, C.-W. Tsai, J. W. H. Niemantsverdriet and E. H. G. Langner, *ACS Omega*, 2021, **6**, 21850–21860.
19 R. D'Amato, A. Donnadio, M. Carta, C. Sangregorio, D. Tiana, R. Vivani, M. Taddei and F. Costantino, *ACS Sustainable Chem. Eng.*, 2019, **7**, 394–402.
20 P. M. Bhatt, Y. Belmabkhout, A. Cadiau, K. Adil, O. Shekhah, A. Shkurenko, L. J. Barbour and M. Eddaoudi, *J. Am. Chem. Soc.*, 2016, **138**, 9301–9307.
21 T.-H. Chen, I. Popov, W. Kaveevivitchai, Y.-C. Chuang, Y.-S. Chen, A. J. Jacobson and O. Š. Miljanić, *Angew. Chem., Int. Ed.*, 2015, **54**, 13902–13906.

22 E. Jo, S. Yang, D. W. Kim and D. W. Kang, *Coord. Chem. Rev.*, 2024, **515**, 215958.
23 M. F. Abbas, Y. L. He, G. Y. Sun, A. B. Sun, E. T. Eldin and S. S. M. Ghoneim, *IEEE Access*, 2023, **11**, 91767–91776.
24 S.-M. Li, Q. Zhang, H.-C. Jiang, Q.-L. Ni, L.-C. Gui, X.-J. Wang and T.-L. Hu, *Chem. Eng. J.*, 2024, **496**, 154026.
25 X. Sun, L. Zhou, J. Chen, Z. Jia, Z. Zhao and Z. Zhao, *J. Mater. Chem. A*, 2025, **13**, 2360–2377.
26 D. K. J. A. Wanigarathna, J. Gao and B. Liu, *Mater. Adv.*, 2020, **1**, 310–320.
27 M. Åhlén, A. Jaworski, M. Strømme and O. Cheung, *Chem. Eng. J.*, 2021, **422**, 130117.
28 G. Han, K. M. Rodriguez, Q. Qian and Z. P. Smith, *Ind. Eng. Chem. Res.*, 2020, **59**, 18139–18150.
29 J. H. Cavka, S. Jakobsen, U. Olsbye, N. Guillou, C. Lamberti, S. Bordiga and K. P. Lillerud, *J. Am. Chem. Soc.*, 2008, **130**, 13850–13851.
30 A. Altomare, C. Cuocci, C. Giacovazzo, A. Moliterni, R. Rizzi, N. Corriero and A. Falcicchio, *J. Appl. Crystallogr.*, 2013, **46**, 1231–1235.
31 S. J. Garibay and S. M. Cohen, *Chem. Commun.*, 2010, **46**, 7700–7702.
32 M. I. Gonzalez, E. D. Bloch, J. A. Mason, S. J. Teat and J. R. Long, *Inorg. Chem.*, 2015, **54**, 2995–3005.
33 D. A. Gómez-Gualdrón, P. Z. Moghadam, J. T. Hupp, O. K. Farha and R. Q. Snurr, *J. Am. Chem. Soc.*, 2016, **138**, 215–224.
34 J. Rouquerol, P. Llewellyn and F. Rouquerol, in *Studies in Surface Science and Catalysis*, ed. P. L. Llewellyn, F. Rodriquez-Reinoso, J. Rouquerol and N. Seaton, Elsevier, Amsterdam, 2007, vol. 160, p. 49.
35 X. Zhu, S. M. Mahurin, S.-H. An, C.-L. Do-Thanh, C. Tian, Y. Li, L. W. Gill, E. W. Hagaman, Z. Bian, J.-H. Zhou, J. Hu, H. Liu and S. Dai, *Chem. Commun.*, 2014, **50**, 7933–7936.
36 X. Zhu, C. Tian, G. M. Veith, C. W. Abney, J. Dehaudt and S. Dai, *J. Am. Chem. Soc.*, 2016, **138**, 11497–11500.
37 J. Schell, N. Casas, R. Pini and M. Mazzotti, *Adsorption*, 2012, **18**, 49–65.
38 S. Lee, J. H. Lee and J. Kim, *Korean J. Chem. Eng.*, 2018, **35**, 214–221.
39 J. Young, F. McIlwaine, B. Smit, S. Garcia and M. van der Spek, *Chem. Eng. J.*, 2023, **456**, 141035.
40 A. Erba, J. K. Desmarais, S. Casassa, B. Civalleri, L. Donà, I. J. Bush, B. Searle, L. Maschio, L. Edith-Daga, A. Cossard, C. Ribaldone, E. Ascrizzi, N. L. Marana, J.-P. Flament and B. Kirtman, *J. Chem. Theory Comput.*, 2023, **19**, 6891–6932.
41 L. Donà, J. G. Brandenburg and B. Civalleri, *J. Chem. Phys.*, 2022, **156**, 094706.
42 L. Doná, J. G. Brandenburg and B. Civalleri, *J. Chem. Phys.*, 2019, **151**, 121101.
43 H. Kruse and S. Grimme, *J. Chem. Phys.*, 2012, **136**, 154101.
44 S. Grimme, J. Antony, S. Ehrlich and H. Krieg, *J. Chem. Phys.*, 2010, **132**, 154104.
45 W. Klemperer and G. C. Pimentel, *J. Chem. Phys.*, 1954, **22**, 1399–1402.
46 N. Fuson, M. L. Josien, E. A. Jones and J. R. Lawson, *J. Chem. Phys.*, 1952, **20**, 1627–1634.
47 L. Li, S. Tang, C. Wang, X. Lv, M. Jiang, H. Wu and X. Zhao, *Chem. Commun.*, 2014, **50**, 2304–2307.
48 C. F. Macrae, I. Sovago, S. J. Cottrell, P. T. A. Galek, P. McCabe, E. Pidcock, M. Platings, G. P. Shields, J. S. Stevens, M. Towler and P. A. Wood, *J. Appl. Crystallogr.*, 2020, **53**, 226–235.
49 J. Ethiraj, E. Albanese, B. Civalleri, J. G. Vitillo, F. Bonino, S. Chavan, G. C. Shearer, K. P. Lillerud and S. Bordiga, *ChemSusChem*, 2014, **7**, 3382–3388.
50 S. Demir, N. Bilgin, H. M. Cepni, H. Furukawa, F. Yilmaz, C. Altintas and S. Keskin, *Dalton Trans.*, 2021, **50**, 16587–16592.
51 D. K. Yoo and S. H. Jhung, *J. Mater. Chem. A*, 2022, **10**, 8856–8865.
52 M.-B. Kim, K.-M. Kim, T.-H. Kim, T.-U. Yoon, E.-J. Kim, J.-H. Kim and Y.-S. Bae, *Chem. Eng. J.*, 2018, **339**, 223–229.
53 M.-B. Kim, T.-H. Kim, T.-U. Yoon, J. H. Kang, J.-H. Kim and Y.-S. Bae, *J. Ind. Eng. Chem.*, 2020, **84**, 179–184.
54 M.-B. Kim, T.-U. Yoon, D.-Y. Hong, S.-Y. Kim, S.-J. Lee, S.-I. Kim, S.-K. Lee, J.-S. Chang and Y.-S. Bae, *Chem. Eng. J.*, 2015, **276**, 315–321.
55 N. S. Wilkins, A. Rajendran and S. Farooq, *Adsorption*, 2021, **27**, 397–422.